The International Archives of the Photogrammetry, Remote Sensing and Spatial Information Sciences, Volume XLVIII-1/W6-2025
3rd International Workshop on Evaluation and BENCHmarking of Sensors, Systems and
GEOspatial Data in Photogrammetry and Remote Sensing (GEOBENCH), 20–21 November 2025, Wroclaw, Poland

Long-Term Monitoring of Small Displacements of Infrastructures with a Low-Cost GNSS Device

Raniero Beber[1], Luca Morelli[1], Mustafa Eid[1], Pawel Trybała[1], Fabio Remondino[1]

[1] 3D Optical Metrology (3DOM) unit, Bruno Kessler Foundation (FBK), Trento, Italy
Web: http://3dom.fbk.eu – Email: <rbeber, lmorelli, meid, ptrybala, remondino>@fbk.eu

Keywords: Positioning, GNSS, Low-Cost, High-precision, RTK, PPK, displacement.

Abstract
The monitoring of large infrastructures such as bridges, dams, and Tailings Storage Facilities (TSFs) is critical for ensuring structural safety and preventing catastrophic failures. Traditional geodetic monitoring approaches, while accurate, are often labour-intensive, expensive, and impractical for large-scale or remote deployments. This study evaluates the capability of dual-frequency low-cost GNSS receivers (ublox ZED-F9R) integrated with a minicomputer to measure millimeter-scale movements over extended monitoring periods. Two measurement campaigns are conducted: a 16-hour short-term test and a 60-day long-term deployment. A rigid aluminium beam with photogrammetrically measured baseline served as ground truth for assessing positioning accuracy. Short-term experiments demonstrated sub-millimeter accuracy while the 60-day campaign achieved 3D baseline measurement accuracy and precision below 2 mm despite significant environmental variations. The results confirm that low-cost dual-frequency GNSS systems can reliably detect centimeter/year-level deformations, making them suitable for monitoring slow-moving processes in critical infrastructure. The collected data, including raw GNSS observations, processed coordinates, and meteorological data, is publicly available for research purposes at https://doi.org/10.5281/zenodo.17378723.

1. Introduction

Aging infrastructures around the world are facing critical but mandatory monitoring challenge. Bridges, dams, and tailings storage facilities can deteriorate silently, with millimeter of movements potentially leading to catastrophic failure. Nowadays infrastructures operate decades beyond design lifetimes and we are witnessing hundreds structural collapses of critical infrastructures per decade (Medaa et al., 2025).
Therefore, continuous millimeter-precision monitoring solutions have become crucial. Traditional geodetic systems (Scaioni et al. 2018), such as robotic total stations, achieve the required accuracy but remain prohibitively expensive, labour-intensive, and operationally complex for widespread deployment. Other approaches include IoT (Bhatta and Dang, 2024), MEMS sensors (Cigada and Lastrico, 2023) or SAR (Bondi et al., 2020).
With the increase availability and affordability of dual-frequency low-cost GNSS receivers, continuous infrastructure monitoring can be operated over extended periods, rivalling geodetic-grade equipment at a fraction of the cost. The implications transcend cost savings. Low-cost GNSS enables dense sensor networks with comprehensive spatial coverage across kilometers, operating autonomously in remote locations while delivering real-time alerts before deformations become critical. Experiences in the SEC4TD[1] project (Beber at al., 2024) - which pioneered IoT positioning with real-time structural modelling for mining safety - pushed authors to investigate further the long-term monitoring of infrastructures with low-cost GNSS devices.

1.1 Aim of the work

This study evaluates low-cost GNSS devices for monitoring slow infrastructure deformations (centimeters/year velocity) over extended periods, demonstrating their viability as affordable alternatives to expensive geodetic equipment for applications like dam monitoring and mining infrastructure. The key objectives of the work include:

- Validate precision: to prove millimeter-level accuracy using dual-antenna systems with baselines from 50 cm to 4 km;
- Enable affordable monitoring: to provide cost-effective solutions for infrastructure health monitoring where budget constraints exist;
- Share open data: to contribute long-term GNSS datasets to the research community for machine learning (ML) algorithm development and validation;
- Support early warning: to detect gradual structural changes before they become critical safety concerns;
- Scale deployment: to enable easy installation and expansion across large structures in harsh/remote environments;
- Dense monitoring network: to deploy multiple low-cost units for comprehensive spatial and temporal coverage.

These objectives converge toward replacing expensive, intermittent, sparse monitoring with affordable, continuous, dense surveying networks that democratize access to safety-critical infrastructure health information.

2. Related works

2.1. From geodetic networks to GNSS-based monitoring

Infrastructure monitoring evolved from labour-intensive optical surveys through robotic total stations to satellite-based continuous positioning. Scaioni et al. (2018) comprehensively reviewed dam deformation monitoring, documenting that traditional geodetic methodologies achieve millimetric precision but suffer critical limitations: discrete control points risk overlooking localized deformations between measurement locations, manual surveys limit temporal resolution, and total stations require line-of-sight plus stable mounting infrastructure. GNSS technology eliminated these constraints, offering comparable accuracy without line-of-sight requirements while demanding specialized personnel only during design and installation phases rather than routine operation (Reguzzoni et al., 2022).
Real-time kinematic (RTK) processing dominates infrastructure applications by delivering immediate positioning for time-sensitive monitoring. For short baselines typical of dam and

[1] https://sec4td.fbk.eu/

bridge monitoring (under several kilometers), double-differencing effectively eliminates atmospheric errors, achieving centimeter to sub-centimeter accuracy (Xi et al., 2023). Reguzzoni et al. (2022) established statistical time series methodologies for extracting deformation signals from noisy observations, demonstrating that appropriate processing compensates for individual receiver limitations and enables reliable movement detection through temporal analysis.

2.2. Low-cost multi-frequency GNSS solutions

Modern affordable multi-frequency, multi-constellation receivers (GPS, GLONASS, Galileo, BeiDou with dual-frequency ionospheric correction) transformed the cost-accuracy landscape. Xue et al. (2023) rigorously assessed low-cost multi-GNSS receiver accuracy for structural monitoring, establishing that modern affordable systems achieve millimeter-scale deformation detection when optimized for multipath mitigation, antenna stability, and processing algorithms. Tunini et al. (2022) validated low-cost GNSS for crustal deformation monitoring, a process demanding extreme precision over extended scales: they demonstrated that appropriate network design enables meaningful contribution to tectonic movement detection. Morelli et al. (2022) developed cost-effective multi-frequency antennas solutions integrating it with camera sensors for navigation and positioning.

2.3. Device integration and communication infrastructure

GNSS convergence with IoT frameworks enabled distributed sensor networks with centralized management, real-time processing, automated alerts, and remote visualization (Huang et al., 2023). Hamza et al. (2023) developed cost-effective solutions for continuous landslide monitoring, addressing power management and autonomous operation challenges their solar-powered stations with cellular communication operate for extended periods acquiring continuous positioning data. Communication protocol selection critically impacts viability: Yao et al. (2022) documented LoRa advantages for infrastructure monitoring including kilometer-scale range, low power consumption enabling months-to-years battery operation, and robust performance in obstructed environments.

2.4. Applications of GNSS in Infrastructure Monitoring

Capabilities of GNSS-based monitoring have been proven in applications in several key types of critical infrastructure:

- *Tailings Storage Facilities:* Clarkson and Williams (2020) identified that conventional TSF monitoring often proves inadequate, with cost and complexity limiting spatial coverage and creating failure-detection blind spots. The SEC4TD project addressed this through purpose-designed GNSS-IoT devices with dual-band receivers, edge-computing RTK correction, long-life batteries, and LoRa communication. Beber et al. (2024) documented 15-day field validation achieving 17 mm horizontal position mean difference (4 mm standard deviation) under real operational scenarios including power-saving modes, with performance validated against high-end geodetic receivers (Topcon AGM-13).
- *Bridge Monitoring*: Xi et al. (2023) developed moving-base RTK-GNSS for railway bridges, addressing train-induced dynamic displacements through synchronized receivers on deck and reference points. Double-differencing eliminated atmospheric effects while preserving relative displacement, achieving sub-centimeter measurement with high temporal resolution for dynamic structural behavior and vibration analysis.
- *Landslide Surveillance:* Lau et al. (2023) deployed hybrid GNSS-accelerometer systems revealing landslide triggering mechanisms related to rainfall, demonstrating that combined position and acceleration data enhances failure dynamics understanding. Marino et al. (2023) integrated soil moisture sensors, piezometers, and GNSS within unified IoT frameworks for pyroclastic slope monitoring. Zuliani et al. (2022) established multi-site GPS networks across northeastern Italy, documenting multi-year operational challenges including power management and communication in mountainous terrain while developing processing methodologies for extracting deformation signals from noisy low-cost observations.
- *Construction Safety:* Ragnoli et al. (2022) combined GNSS with inertial readings and RFID for real-time worker tracking and hazard alerting via LoRa communication, demonstrating platform versatility beyond structural deformation measurement.

2.5. Processing methodologies and persistent challenges

The European Plate Observing System[2] established processing standards for long-term position time series including outlier detection, discontinuity identification, and velocity estimation. Reguzzoni et al. (2022) applied autoregressive models and seasonal decomposition to separate thermal effects, seasonal loading, and structural movements, providing frameworks for automated anomaly detection.
Critical research gaps persist:

- *Long-term stability*: most studies span days to months while infrastructure demands years to decades of reliability;
- *Environmental robustness*: comprehensive characterization of temperature, precipitation, EMI, and multipath effects across diverse scenarios remains incomplete;
- *Processing optimization*: trade-offs between complexity, computational requirements, and accuracy need systematic evaluation for resource-constrained edge computing;
- *Validation methodologies*: establishing sub-centimeter ground truth over extended periods presents substantial challenges, with most studies relying on geodetic-grade equipment comparison rather than independent techniques;
- *Scalable data pipelines*: continuous multi-station monitoring generates substantial volumes requiring efficient transmission, processing, and visualization;
- *Failure detection algorithms*: translating position time series into actionable alerts requires sophisticated methods distinguishing structural concerns from environmental effects and measurement artifacts.

3. Methodology

3.1 Hardware configuration and system architecture

The proposed monitoring solution employs a dual-frequency ublox ZED-F9R receiver connected to a SparkFun TOP106 antenna and operated by a Raspberry Pi 4B (Figure 1a). The ZED-F9R module supports concurrent reception of GPS L1C/A and L2C signals, as well as Galileo E1 and E5b frequencies, enabling ionospheric delay mitigation—one of the primary error sources in GNSS positioning for millimeter-level precision

[2] EPOS, 2025. European Plate Observing System, https://doi.org/10.60888/EPOS-GNSS-Guidelines-Station

applications. The SparkFun TOP106 antenna features a ceramic patch element with integrated low-noise amplifier (LNA), providing stable phase centre characteristics across the L1 and L5/E5b frequency bands with adequate multipath rejection capabilities. During this initial development phase focused on long-term accuracy testing, data are logged locally to onboard storage to ensure complete data integrity and eliminate potential transmission-related gaps. In a future operational phase, following accuracy validation, wireless data transmission over LoRa will be implemented. LoRa technology has been selected for its extended transmission range (several kilometers in open terrain), low power consumption compatible with battery operation, and reliable performance in challenging radio frequency environments, enabling integration with cloud-based data management platforms for real-time visualization and automated alert generation.

3.2 Experimental setup and test configuration

The testing is conducted using the setup shown in Figure 1. Two SparkFun TOP106 antennas are mounted on a rigid aluminium beam (hereafter AL-beam) to maintain constant relative distance during measurements. This fixed-baseline configuration provides an absolute reference for evaluating GNSS positioning performance, as any deviation from the known antenna separation can be directly attributed to measurement error. The AL-beam is mounted on a professional-grade surveying tripod positioned on stable ground, ensuring stable antenna positioning throughout the measurement period.

By adopting a rigid aluminium beam as mount for two GNSS antennas, the error in relative positioning is measured by comparing against the known distance of this rigid baseline. The main variable affecting this distance is the temperature gradient which could cause the beam to expand or contract due to thermal effects. With a maximum temperature gradient of 20°C during the experimentation phase, a maximum elongation of 0.25 mm is estimated based on aluminium's coefficient of thermal expansion (approximately 23×10^{-6} °C^{-1}). This sub-millimeter variation is negligible compared to the multi-millimeter positioning accuracy targets and validates that observed positioning variations significantly exceeding this value can be attributed to GNSS measurement errors.

The antennas are connected to two separate ublox ZED-F9R GNSS receivers orchestrated by a Raspberry Pi 4B for synchronized data acquisition. The receivers are configured via u-center software to log L1/L2 observations from GPS and GALILEO constellations at 1 Hz sampling rate. This dual-constellation approach increases satellite visibility and improves geometric diversity, enhancing positioning solution robustness. Linux routines have been implemented to make the entire data acquisition pipeline automatic starting from boot when the mini-computer is plugged into the power bank, ensuring autonomous operation with minimal manual intervention.

3.3 Measurement campaigns

As shown in Figure 1, the AL-beam is fixed to a professional tripod on stable ground. Two measurement campaigns are conducted: the short-term campaign acquired data (at a 1 Hz) for 16 hours from May 20th, 2025 at 14:46:00 to May 21st, 2025 at 06:48:43, at approximately 46°03'59.8"N, 11°09'09.3"E, designed to assess measurement precision while capturing at least one complete orbital repeat cycle. The long-term campaign collected continuous data for 60 days from May 30th, 2025 to July 29th, 2025 at approximately 46°04'01.3"N, 11°09'04.6"E, enabling assessment of measurement stability across seasonal atmospheric variations, temperature cycles, and evolving satellite constellation configurations.

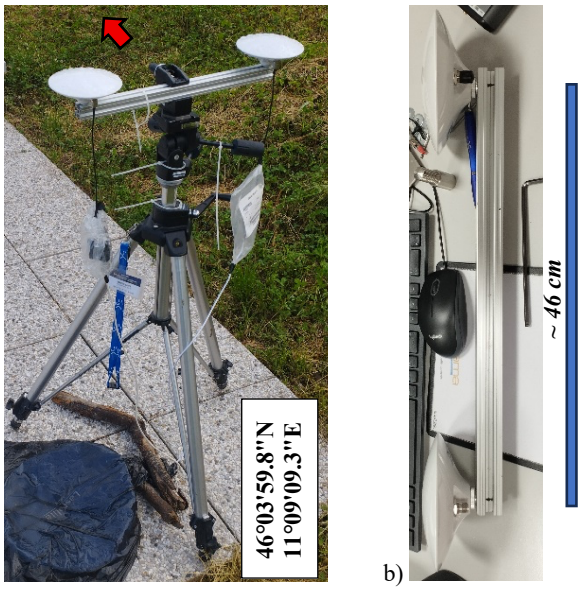

a) b)

Figure 1. a) GNSS full setup with a fixed baseline: two TOP106 antennas (i.e. A & B), two ZED-F9R receivers, the Raspberry Pi to automate the logging process. The red arrow indicates North direction nearly perpendicular to the Al-beam; b) Antenna mount detail with rigid AL-beam as baseline.

(a) (b)

Figure 2. Photogrammetric 3D survey of the AL-beam to precisely measure the rigid distance between the two GNSS antennas. Acquisition setup (a) and detail of the antenna connectors with their centres (b).

3.4 AL-beam measurements as Ground Truth

To ensure the highest accuracy in the definition of the AL-beam length (i.e., the distance between the two antenna reference points), a photogrammetric pipeline is adopted to measure its length both before and after the GNSS logging campaigns.

Two calibration boards featuring coded targets with known dimensions are positioned on the ground plane alongside the AL-beam (Figure 2a) and used to scale the photogrammetric reconstruction. From a set of 37 convergent images acquired around the setup, a photogrammetric model is generated and accurately scaled using the known distances between targets on the calibration boards. This approach enabled reliable estimation of the beam's length with sub-millimeter precision (Figure 1b). Four scale bars with precisely known distances are incorporated into the calibration setup. Two scale bars are used to establish the metric scale of the photogrammetric model, while the remaining two served as independent check measurements to verify reconstruction accuracy. The check scale bars yielded an average residual error of 0.12 mm, demonstrating the high precision of the photogrammetric measurement. The ground truth distance

between the two GNSS antenna reference points on the rigid AL-beam is determined to be 465.65 mm, establishing the baseline reference for evaluating relative positioning accuracy throughout the GNSS measurement campaigns.

3.5 GNSS data processing strategy

The GNSS observations are processed using RTKLIB (Takasu, 2009) in post-processed kinematic (PPK) mode on our DICLUB[3] High-Performance Computing (HPC) facility.
The proposed dual-receiver setup is evaluated under two distinct scenarios: (a) processing with a nearby local permanent GNSS station (within a maximum of 10 km from the rover), simulating typical monitoring applications where existing geodetic infrastructure can be leveraged, and (b) operation in a remote area with no installed permanent station, employing two low-cost receivers where one acts as base and the other as rover, representing autonomous monitoring in isolated locations.
In Scenario (a), dual-frequency (L1/L2) observations from the Monte Calisio permanent station (MOCA, located approximately 4 km from the test site) are used to independently estimate positions for each receiver (Rover_A and Rover_B). In Scenario (b), the two receivers alternately served as base and rover to ensure measurement consistency and eliminate potential receiver-specific biases. For both scenarios, positions are estimated and the 3D baseline distance between the two antennas is computed and compared against the known physical baseline length of 465.65 mm. Both scenarios are evaluated under two temporal processing approaches: (i) single block processing, where the full 16-hour GNSS data block is processed as a single continuous solution of which the median of the latest 5 fix is used as position, and (ii) segmented processing, where PPK is performed over consecutive 1-hour GNSS data blocks, using the median of the latest 5 fix as representative to simulate operational monitoring conditions requiring periodic position updates.
For the long-term acquisition campaign (60 days), only scenario (a) with the ii) temporal processing schema is investigated due to computational constraints and because it represents the more challenging baseline configuration (4 km vs. 0.5 m). Moreover, case ii) employs a data processing method that provides hourly position estimates, thereby enabling emergency alerts with maximum delay of one hour, considerate acceptable for slow-moving processes.

3.6 Evaluation metrics

The evaluation is conducted at two hierarchical levels to assess both overall accuracy and temporal stability. First, the photogrammetric ground truth of the AL-beam distance is compared with the 3D baseline distance between the two antennas computed by PPK processing of the full 16-hour dataset. Second, the GNSS raw data are segmented into 1-hour blocks and processed independently to evaluate measurement consistency over time and assess the system's capability for operational monitoring with periodic position updates.
The individual coordinate components (ENU in local topocentric frame) of the baseline vector between Antenna A and Antenna B are reported in the results primarily as indicators of setup alignment. Specifically, the East-North components reflect the beam's orientation relative to cardinal directions, while the vertical component (Up) indicates the levelness of the beam. However, these individual components are not the primary evaluation metric, as the physical constraint of the rigid AL-beam ensures that only the 3D baseline length, calculated as the Euclidean norm of the positioning components, represents the invariant distance between the two antennas. Any deviations of this distance from the ground truth value directly quantify the combined positioning error of the dual-receiver system.

4. Short-term results

The short-term tests are divided into two main experiments:
a) testing 4 km baseline between MOCA and the two rovers (i.e. rover_A and rover_B);
b) testing the short baseline (~50 cm) using antenna A & B as base and rover (i.e. base_A & rover_B and base_B & rover_A).
In both experiments the number of processed observations in PPK are reduced from 57600 (i.e. 16h) to 3600 (i.e. 1h) to show time flexibility of the solution.

4.1 PPK processing of rover_A and rover_B with MOCA base station in ENU

The results of processing 16 h observations are reported in Table 1 in terms of estimated distance (i.e. D. 3D), that compared with ground truth distance shows an error of 0.03 mm. Figure 3 report instead the same comparison when PPK is performed over 1h blocks. In this case the average error is of 0.44 mm with a standard deviation of 1.19mm as reported in Table 1. The comparison of the results indicates that hourly processing attains, on average, a level of sub-millimeter accuracy comparable to that of 16-hour processing, with a precision marginally exceeding 1 mm.

Processing	D. 3D	GT	Error
16h block	465.68	465.65	0.03
Average of 16 1h blocks	465.21 ± 1.19		0.44

Table 1. PPK solution comparison (in mm) for vector difference of absolute positioning of rover_A & rover_B with MOCA as base station in ENU reported as full 16h block processing or hour by hour.

Figure 3. PPK solution comparison (in mm) by processing rover_A & rover_B as separate entities and computing the distance vector in ENU coordinates in 1h time blocks.

	Processing	D. 3D	GT	Error
base_A rover_B & vice-versa	16h block	465.67	465.65	0.02
	16x 1h blocks	465.46 ±1.06		0.19

Table 2. PPK solution comparison (in mm) from base_A, rover_B and vice-versa with materialization from MOCA base station with processing the full 16h block or the 16 blocks of one hour each.

[3] https://dicenter.fbk.eu/labs-and-hpc

4.2 PPK processing from base_A, rover_B and vice-versa with materialization from MOCA base station

Table 2 reports the 3D distance computed between the two receivers, one playing as base and the other one as rover and vice-versa of the PPK processing between the two antennas. The error processing the full 16h block is 0.02 mm while it increases to 0.19 mm for the 16 blocks of one hour each.
Figure 4 shows the results of the 1h blocks position estimates reported as individual components (ENU) and estimated distance compared to the known baseline. Table 2 summarizes the performance over the short baseline at 1h processing. Similarly to the previous section, the precision of the hourly processing is at millimeter level, while the 16h processing is almost ten times more accurate respects the hourly processing.

Figure 4. PPK solution comparison (in mm) by processing rover_A & rover_B and vice-versa with materialization from MOCA base station in 1h time blocks.

5. Long-term results

As demonstrated in the previous section, sub-millimeter errors are obtained for both baseline scenario (0.5 m and 4 km). However, since this configuration does not represent realistic operational conditions, the actual long-term testing is performed using MOCA as the base station (approximately 4 km baseline), with the 3D distance computed as the vector length between the two rovers.
The 60-day acquisition period experienced strong wind gusts that tilted the tripod on one occasion (July 1, 2025). Consequently, data from June 30, 2025 at 23:59 to July 2, 2025 at 18:00 are excluded from the statistical metrics, and the long-term analysis is split into pre-event and post-event periods. Nevertheless, the complete dataset, including the excluded period, is available in the public repository for further processing and investigation. Table 3 reports summary statistics for all individual fixed solutions at 1 Hz and Table 4 shows median positions within 1h time windows.
Figure 5 presents seven time-series subplots summarizing the experimental results. The first six subplots display the ENU (East, North, Up) coordinates referenced to the MOCA base station for Rover_A and Rover_B. In each subplot, grey points represent all individual fixed solutions obtained at 1 Hz from PPK processing of each 1-hour observation block. Colored points indicate the hourly median of all fixed solutions, while the black line shows a 24-hour moving average of the median positions. The bottom subplot displays the 3D baseline distance computed from the hourly median ENU positions, the photogrammetric ground truth (0.46565 m, dashed line), and a 24-hour moving average (orange line).

	pre-event μ [m] ± σ [mm]		post-event μ [m] ± σ [mm]	
	Rover A	**Rover B**	**Rover A**	**Rover B**
# SAMPLE	1671932 [-]		1385125 [-]	
EAST	607.302 ± 5.28	606.838 ± 5.26	607.290 ± 4.15	606.825 ± 4.21
NORTH	-3459.370 ± 6.81	-3459.376 ± 6.81	-3459.415 ± 5.70	-3459.415 ± 5.61
UP	-704.401 ± 19.70	-704.393 ± 19.95	-704.407 ± 22.48	-704.403 ± 22.82
3D DIST.	0.46416 ± 1.72		0.46438 ± 1.61	
3D DIST. ERROR	1.49 [mm]		1.26 [mm]	
3D DIST. ERROR full	1.38 [mm]			

Table 3. Summary metrics for all fixed positions processed at 1 Hz for the long-term testing (i.e. 60 days) reported for pre- and post-event.

	pre-event μ [m] ± σ [mm]		post-event μ [m] ± σ [mm]	
	Rover A	**Rover B**	**Rover A**	**Rover B**
# MEDIAN SAMPLE	517 [-]		445 [-]	
EAST	607.302 ± 4.65	606.838 ± 4.58	607.290 ± 3.89	606.825 ± 3.83
NORTH	-3459.365 ± 6.23	-3459.376 ± 6.25	-3459.416 ±5.29	-3459.417 ± 5.18
UP	-704.400 ± 19.13	-704.394 ± 19.28	-704.409 ± 21.93	-704.403 ± 22.09
3D DIST.	0.4641 ± 1.38		0.46442 ± 1.45	
3D DIST. ERROR	1.55 [mm]		1.22 [mm]	
3D DIST. ERROR full	1.40 [mm]			

Table 4. Summary metrics hourly median positions for the long-term testing (i.e., 60 days) reported for pre- and post-event.

No major systematic differences are observed between the ENU coordinates of Rover_A and Rover_B referenced to MOCA; however, the three coordinate components exhibit different noise characteristics. For the East component, all fixed solutions span a range of approximately 50 mm over the full period. The East component shows standard deviations of 5.26 mm and 5.25 mm for Rover_A and Rover_B during the pre-event period, improving to 4.16 mm and 4.22 mm in the post-event period. When considering hourly medians instead of all individual fixes (Table 4), the precision improves to 4.65 mm and 4.58 mm for the pre-event period, and 3.89 mm and 3.83 mm for the post-event period, representing improvements of approximately 0.6-0.7 mm.
The North component exhibits similar behaviour. Table 3 shows standard deviations of 6.81 mm for both rovers during the pre-event period, reducing to approximately 5.65 mm in the post-event period. Hourly median processing (Table 4) further reduces the standard deviation by approximately 0.6 mm during the pre-event period (from 6.81 mm to ~6.24 mm) and by 0.5 mm during the post-event period (from ~5.65 mm to ~5.24 mm).
In contrast, the Up component shows substantially higher noise levels, with standard deviations around 20 mm for all fixed solutions (Table 3) and remaining close to 19-22 mm even after hourly median filtering (Table 4). Despite multiple reprocessing attempts with different filtering parameters, no configuration yielded significantly reduced vertical noise.

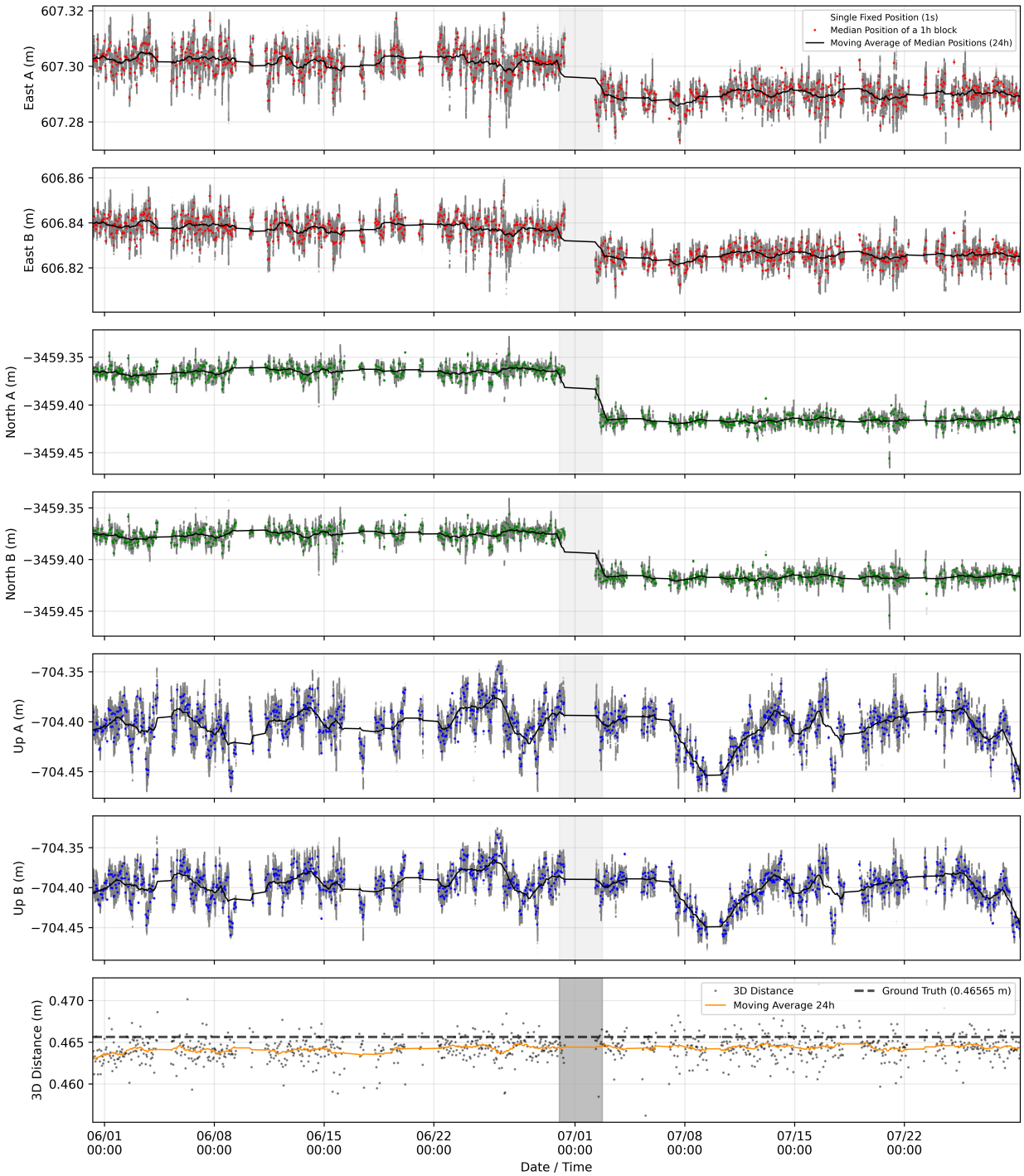

Figure 5. Time series of ENU coordinates of rover_A (odd subplots) and rover_B (even plots) and the 3D baseline distance (bottom) for the 60-day monitoring campaign. The grey shaded area (July 1, 2025) indicates the period excluded from analysis due to tripod displacement caused by strong wind gusts.

In line with the primary focus of this study, i.e. evaluating performance against the AL-beam baseline distance between the two rovers using the photogrammetric measurement as ground truth, the 3D distance results demonstrate excellent performance: Table 3 shows that using all individual fixed solutions yields standard deviations of 1.72 mm (pre-event) and 1.61 mm (post-event), with absolute errors of 1.49 mm and 1.27 mm respectively. The hourly median processing (Table 4) improves precision to 1.38 mm (pre-event) and 1.45 mm (post-event), with absolute errors of 1.56 mm and 1.21 mm. When considering the combined full dataset, the overall 3D distance error is 1.38 mm (Table 3) and 1.40 mm (Table 4), demonstrating that the low-cost dual-receiver system can reliably measure the known baseline with millimeter accuracy over extended periods, even with a 4 km separation from the reference station.

The Up time series reveals multi-day trends (Figure 6) with fluctuations spanning approximately 10 cm over the full 60-day period, likely attributable mostly to atmospheric modelling limitations, tropospheric delay variations, and satellite geometry changes. Figure 6 demonstrates a spectrogram of the Fast Fourier Transform of the 6 component and the 3D distance split in pre- and post-event. The dominance around 1-day period for the Up

component is clear; in the horizontal coordinates a frequency change with time is observe for higher periods suggesting interplay with external factors from the solely GNSS processing.

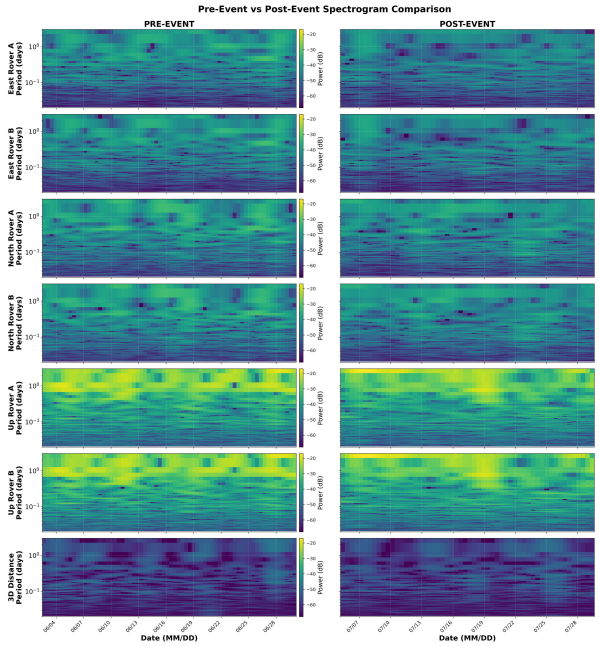

Figure 6. Pre- and post-event spectrogram comparison on fixed positions 15 minutes median.

5.1 De-trend residuals standard deviation analysis

To better characterize the behaviour of the ENU coordinates over the two months, the 1 Hz fixed solutions is detrended by a moving average with window size of 1, 3, 6, 12, 24, 72h as well as 1 and 2 weeks and 1 month. Figure 7 presents the results of detrending analysis applied to the ENU coordinates and 3D distance, comparing standard deviation of the residuals in the pre- and post-event periods for the two rovers. Four subplots show the East, North, and Up components, along with the estimated 3D baseline distance, as a function of moving average window size ranging from 1 hour to 1 month.

For the East component (top panel), both rovers show a clear decrease in standard deviation as the moving average window decreases. Pre-event values start around 2 mm for the 1-hour window and stabilize around 5 mm for longer windows. Post-event performance shows similar behaviour, with Rover A exhibiting slightly lower variability (~4 mm) compared to Rover B (~4.2 mm) at longer window sizes. The convergence beyond the 72-hour window suggests that multi-day trends have been effectively removed and that good part of the variability is due to factors varying with a lower frequency.

The North component (second panel) exhibits similar patterns to the East component. Pre-event standard deviations begin around 3 mm for short windows and converge to approximately 6.8 mm for both rovers at longer averaging periods. Post-event results show nearly identical behaviour, with both rovers stabilizing around 5.7-5.8 mm. The similarity between East and North components indicates consistent horizontal positioning performance.

In stark contrast, the Up component (third panel) shows substantially higher noise levels and different scaling behaviour. Standard deviations start around 6-7 mm for 1-hour windows and increase dramatically to approximately 20-23 mm for 1-month windows. This increasing trend with window size confirms the presence of strong multi-day systematic effects in the vertical component, consistent with the ~1-2 days periodicity identified in the Short-Time Fourier Transform analysis mentioned previously. Pre-event Rover B shows slightly higher values (~23 mm) compared to other configurations (~20 mm) at the longest window sizes. This behavior indicates a need to introduce correction models, either physics-based (Wei et al., 2025), or ML-based (Crocetti et al., 2025), to further reduce the influence of currently unmodeled factors and retain the short-term precision of the solution also in months-long monitoring scenarios.

The 3D baseline distance (bottom panel) shows the most stable and consistent behaviour. Both pre-event and post-event distances remain constant across all window sizes bigger than 6h, hovering around 1.6 mm. The distance standard deviation shows minimal sensitivity to the detrending window, increasing only slightly from ~1.2 mm to ~1.7 mm as window size increases from 1 hour to 1 month. This stability is particularly significant because it demonstrates that the relative positioning between the two rovers is largely immune to the multi-day systematic effects that plague the baseline vector components.

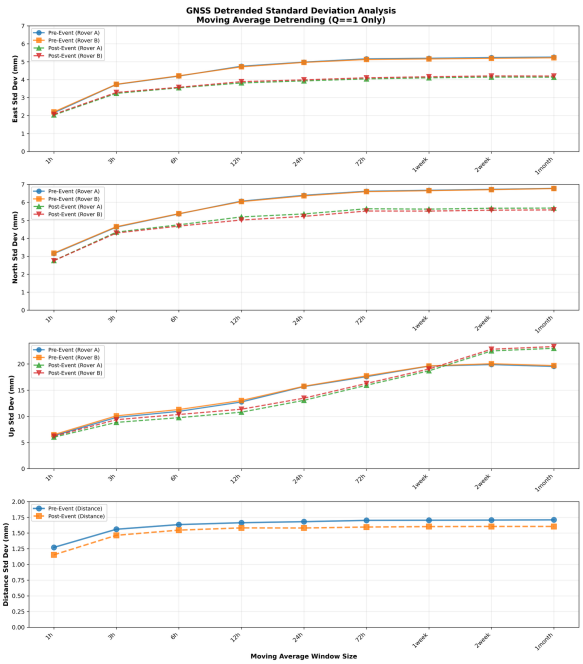

Figure 7. Standard deviation of ENU coordinates and distance residuals after Moving Average (MA) detrending at different time windows for the pre- and post-event periods.

6. Conclusions

This work demonstrates the capability of dual-frequency low-cost GNSS receivers (ublox ZED-F9R) to measure small deformations of large infrastructures with millimetric precision. Short-term experiments achieved millimeter-level accuracy for intra-rover distance at a short baseline, with precision consistently around 1 mm also across longer baseline configurations and temporal processing strategies.

The extended 60-day monitoring campaign validates long-term measurement stability under realistic operational conditions. Analysis of over 3 million fixed solutions demonstrates that the dual-receiver system maintains 3D baseline measurement accuracy of approximately 1.4 mm against the photogrammetric ground truth, with precision of 1.4 mm for hourly medians. This performance is sustained despite significant environmental variations including 20°C temperature fluctuations and a severe wind gusts. The single horizontal components over a 4 km

baseline (East and North) exhibit standard deviations of 4-6 mm, while the vertical component shows higher noise levels (19-22 mm).

The presented results confirm that the proposed low-cost GNSS solution can reliably detect deformations at the level of centimeters per year for the horizontal components, making it suitable for monitoring slow-moving processes or gradual structural changes in critical infrastructure such as TSF, dams, and bridges. The combination of autonomous operation, minimal maintenance requirements, scalability, and proven millimetric accuracy positions the proposed solution as a cost-effective alternative to traditional geodetic monitoring systems for long-term infrastructure surveillance and early warning applications. All data used in the presented experiments are publicly available[4].

References

Bhatta, S. and Dang, J., 2024. Use of IoT for structural health monitoring of civil engineering structures: a state-of-the-art review. *Urban Lifeline*, Vol. 2(17).

Beber, R., Morelli, L., Remondino, F., Hernandez, F., 2024. An IoT-based GNSS platform for infrastructure monitoring. *Int. Arch. Photogramm. Remote Sens. Spatial Inf. Sci*., XLVIII-2/W8, 17-23.

Bondi, F., Addabbo, P., Ullo, S.L., Clemente, C., Orlando, D., 2020. Perspective on the structural health monitoring of bridges by Synthetic Aperture Radar. *Remote Sensing*, 23, p. 3852.

Cigada, A., and Lastrico, G., 2023. Concrete bridges continuous SHM using MEMS sensors:anomaly detection for preventive maintenance. *Lecture Notes in Civil Eng*., Vol. 253.

Clarkson, L. and Williams, D., 2020. Critical review of tailings dam monitoring best practice. *International Journal of Mining, Reclamation and Environment*, 34(2), pp.119-148.

Crocetti, L., Schartner, M., Schneider, R., Schindler, K., Soja, B., 2025. Correction Models for GNSS Displacements in Europe based on Environmental Variables and XGBoost. *Authorea Preprints*.

Hamza, V., Stopar, B., Sterle, O., Pavlovčič-Prešeren, P., 2023. A cost-effective GNSS solution for continuous monitoring of landslides. *Remote Sensing,* 15(9), p.2287.

Huang, G., Du, S., Wang, D., 2023. GNSS techniques for real-time monitoring of landslides: A review. *Satellite Navigation*, 4(1), p.5.

Lau, Y.M., Wang, K.L., Wang, Y.H., Yiu, W.H., Ooi, G.H., Tan, P.S., Wu, J., Leung, M.L., Lui, H.L., Chen, C.W., 2023. Monitoring of rainfall-induced landslides at Songmao and Lushan, Taiwan, using IoT and big data-based monitoring system. *Landslides*, 20(2), pp. 271-296.

Marino, P., Roman Quintero, D.C., Santonastaso, G.F., Greco, R., 2023. Prototype of an IoT-based low-cost sensor network for the hydrological monitoring of landslide-prone areas. *Sensors*, 23(4), p.2299.

Medaa, E., Javid, A.A.S., Malekitabar, H., 2025. Evolution of risk analysis in construction disaster: a systematic Review of construction accidents from 2010 to 2025. *Buildings*, 15(2).

Morelli, L., Menna, F., Vitti, A., Remondino, F., 2022. Action cams and low-cost multi-frequency antennas for GNSS assisted photogrammetric applications without ground control points. *Int. Arch. Photogramm. Remote Sens. Spatial Inf. Sci*., XLVIII-2/W1-2022, pp.171-176.

Oniga, E., Boroianu, B., Morelli, L., Remondino, F., Macovei, M., 2024. Beyond ground control points: cost-effective 3D building reconstruction through gnss-integrated photogrammetry. *Int. Arch. Photogramm. Remote Sens. Spatial Inf. Sci*., XLVIII-2/W4-2024, 333–339.

Ragnoli, M., Colaiuda, D., Leoni, A., Ferri, G., Barile, G., Rotilio, M., Laurini, E., De Berardinis, P., Stornelli, V., 2022. A LoRaWAN multi-technological architecture for construction site monitoring. *Sensors*, 22(22), p.8685.

Reguzzoni, M., Rossi, L., De Gaetani, C.I., Caldera, S., Barzaghi, R., 2022. GNSS-based dam monitoring: The application of a statistical approach for time series analysis to a case study. *Applied Sciences*, *12*(19), p.9981.

Scaioni, M., Marsella, M., Crosetto, M., Tornatore, V., Wang, J., 2018. Geodetic and remote-sensing sensors for dam deformation monitoring. *Sensors*, *18*(11), p.3682.

Takasu, T., 2013. Rtklib. Available: http:\\www. rtklib. com.

Tunini, L., Zuliani, D., Magrin, A., 2022. Applicability of cost-effective GNSS sensors for crustal deformation studies. *Sensors*, 22(1), p.350.

Vadlamudi, M.N., Jayanthi, N., Swetha, G., Nishitha, P., Al-Salman, G.A., Saikumar, K., 2024. IoT Empowered GNSS Tracking in Real-time via Cloud Infrastructure. *Proc. IEEE 9th Int. Conference for Convergence in Technology*, pp. 1-6.

Xi, R., Jiang, W., Xuan, W., Xu, D., Yang, J., He, L., Ma, J., 2023. Performance Assessment of Structural Monitoring of a Dedicated High-Speed Railway Bridge Using a Moving-Base RTK-GNSS Method. *Remote Sensing*, 15(12), p.3132.

Xue, C., Psimoulis, P., Horsfall, A., Zhang, Q., Meng, X., 2023. Assessment of the accuracy of low-cost multi-GNSS receivers in monitoring dynamic response of structures. *Applied Geomatics,* 15(2), pp.315-326.

Walker, S., 2015. Tailings management strategies to meet today's demands. *Engineering and Mining Journal*, 216(11), p.44.

Wei, N., Zhou, Y., Shi, C., Xu, X., Rebischung, P., Liu, J., 2025. Toward a refined estimation of geocenter motion from GNSS displacements: Mitigating thermoelastic deformation and systematic errors. *Journal of Geophysical Research: Solid Earth*, 130(7), e2024JB028967.

Yao, F., Ding, Y., Hong, S., Yang, S.H., 2022. A survey on evolved LoRa-based communication technologies for emerging internet of things applications. *International Journal of Network Dynamics and Intelligence*, pp.4-19.

Zuliani, D., Tunini, L., Di Traglia, F., Chersich, M., Curone, D., 2022. Cost-effective, single-frequency GPS network as a tool for landslide monitoring. *Sensors*, 22(9), p.352.

[4] https://doi.org/10.5281/zenodo.17378723